Gan, Juanjuan; Hou, Nianjun; Yao, Tongtong; Fan, Lijun; Gan, Tian; Huang, Zhiyong; Zhao, Yicheng; Li, Yongdan

A high performing perovskite cathode with in situ exsolved Co nanoparticles for H_2O and CO_2 solid oxide electrolysis cell

Published in:
Catalysis Today

DOI:
10.1016/j.cattod.2020.06.082

Published: 15/03/2021

Document Version
Peer-reviewed accepted author manuscript, also known as Final accepted manuscript or Post-print

Please cite the original version:
Gan, J., Hou, N., Yao, T., Fan, L., Gan, T., Huang, Z., Zhao, Y., & Li, Y. (2021). A high performing perovskite cathode with in situ exsolved Co nanoparticles for H_2O and CO_2 solid oxide electrolysis cell. *Catalysis Today*, *364*, 89-96. https://doi.org/10.1016/j.cattod.2020.06.082

A high performing perovskite cathode with *in situ* exsolved Co nanoparticles for H_2O and CO_2 solid oxide electrolysis cell

Juanjuan Gan,[ab] Nianjun Hou,[ab] Tongtong Yao,[ab] Lijun Fan,[ab] Tian Gan,[ab] Zhiyong Huang,[ab]
Yicheng Zhao,*[ab] Yongdan Li[abc]

[a]State Key Laboratory of Chemical Engineering (Tianjin University), Tianjin Key Laboratory of Applied Catalysis Science and Technology, School of Chemical Engineering and Technology, Tianjin University, Tianjin 300072, China

[b]Collaborative Innovation Center of Chemical Science and Engineering (Tianjin), Tianjin 300072, China

[c]Department of Chemical and Metallurgical Engineering, School of Chemical Engineering, Aalto University, Kemistintie 1, Espoo, P.O. Box 16100, FI-00076 Aalto, Finland

*Corresponding author. Email: zhaoyicheng@tju.edu.cn; Tel: +86-22-27405613; Fax: +86-22-27405243

Abstract

$La_{0.5}Ba_{0.5}Mn_{1-x}Co_xO_{3-\delta}$ ($x < 0.4$) with a perovskite structure is studied as a cathode material for solid oxide electrolysis cells. The exsolution of metallic Co from the perovskite in a reducing atmosphere is in situ investigated. Co improves the electrical conductivity of $La_{0.5}Ba_{0.5}MnO_{3-\delta}$ in a reducing atmosphere, and facilitates the oxygen exchange reaction on the cathode surface. The cathode with in situ exsolved Co nanoparticles shows a high activity for both H_2O and CO_2 electrolysis. At 1.3 V, a single cell supported by a $La_{0.8}Sr_{0.2}Ga_{0.8}Mg_{0.2}O_{3-\delta}$ electrolyte layer achieves H_2O electrolysis current densities of 0.46 and 1.01 A cm^{-2} at 700 and 800 °C, respectively. A high CO_2 electrolysis current density of 0.88 A cm^{-2} is also obtained with the same cell at 1.2 V and 850 °C with a Faradaic efficiency exceeding 90%. The cathode exhibits a high stability for H_2O and CO_2 electrolysis. The co-electrolysis of H_2O and CO_2 with the cathode is also studied.

Keywords: Cathode; Solid oxide electrolysis cell; Co doping; $La_{0.5}Ba_{0.5}MnO_{3-\delta}$

1. Introduction

The massive consumption of fossil fuels brings a growing concern on the removal of the main greenhouse gas CO_2. Meanwhile, the rapid depletion of fossil fuels drives the utilization of renewable energy sources such as wind and solar energy urgently. However, the intermittent nature of those sustainable power sources requires reliable techniques for energy storage and conversion. As a promising strategy for energy storage, the electrochemical conversion of H_2O and CO_2 to H_2 and CO with solid oxide electrolysis cells (SOECs) has been widely studied [1, 2]. Moreover, increasing attention has been focused on the co-electrolysis of H_2O and CO_2 to syngas recently, by which the utilization of excess electricity, the production of basic chemicals and the elimination of CO_2 are realized simultaneously [3, 4].

The cathode material catalyzing the electrochemical reduction of H_2O and CO_2 plays an important role in SOECs. Ni-based cermet materials have been widely used as the cathodes of SOECs due to their high catalytic activity and sufficient electrical conductivity [5]. However, Ni is easily oxidized under a high oxygen partial pressure. Carbon deposition on Ni is another serious problem during CO_2 electrolysis, leading to the rapid degradation of the cathode [4]. The alloying of Ni with other metals such as Fe and Cu can improve the activity and stability of the cathodes for CO_2 electrolysis [6, 7]. Perovskite oxides with a mixed ionic-electronic conductivity are also promising cathode materials. Doped $La_{0.5}Sr_{0.5}FeO_{3-\delta}$ cathode shows a good redox stability and a high coking resistance during pure CO_2 electrolysis and H_2O-CO_2 co-electrolysis [8, 9]. $Sr_2Fe_{1.5}Mo_{0.5}O_{6-\delta}$ with a double-perovskite structure is also studied as the cathode material [10], and its catalytic activity is enhanced with the addition of excessive Fe and the partial substitution of O by F [11, 12].

The in situ exsolution of transition metal nanoparticles in a reducing atmosphere is an effective way to improve the activity of perovskite catalysts. That strategy has been used in the design of fuel electrode materials for solid oxide fuel cells (SOFCs) and SOECs in recent years [13-15]. Tsekouras et al. [16] found that Fe and Ni doped in $La_{0.4}Sr_{0.4}TiO_{3-\delta}$ can be exsolved during reduction, which lower the activation barrier to steam electrolysis remarkably. Ye et al. [17] proved that the chemical adsorption and activation of CO_2 on doped $La_{0.2}Sr_{0.8}TiO_{3+\delta}$ is significantly improved with the exsolution of Ni nanoparticles from the main perovskite. The NiCu alloy exsolved on the surface of $(La_{0.75}Sr_{0.25})_{0.9}(Cr_{0.5}Mn_{0.5})_{0.9}(Ni_{1-x}Cu_x)_{0.1}O_3$ also accelerates the adsorption and activation of CO_2 [18]. $La_{0.43}Ca_{0.37}TiO_3$ with exsolved Ni shows a high stability in a H_2O-CO_2 co-electrolysis cell, and the H_2/CO ratio in the syngas produced is adjustable [4]. The exsolution of Ni nanoparticles is accelerated by electrical reduction with an applied potential [19]. The control of the H_2/CO ratio is also achieved with a co-electrolysis cell using a Ni/Co co-doped $La_{0.7}Sr_{0.2}FeO_3$ cathode by tuning the contents of Ni and Co [20]. Furthermore, the exsolution strategy has been used to improve the performance of layered-perovskite electrode materials such as $La_{1.2}Sr_{0.8}Co_{0.4}Mn_{0.6}O_4$ and $(Pr_{0.4}Sr_{0.6})_3(Fe_{0.85}Mo_{0.15})_2O_7$ [21, 22].

Despite the rapid progress on cathode materials in recent years, their activity and stability are still the key factors limiting the development of SOECs. Double-perovskite $PrBaMn_2O_{5+\delta}$ shows high activity and carbon resistance in SOFCs with H_2 and C_3H_8 as the fuels [23]. It has been also studied as the cathode material of H_2O and CO_2 SOECs [24, 25]. Recently, doped $La_{0.5}Ba_{0.5}MnO_{3-\delta}$ with exsolved Co-Fe nanoparticles has been developed as an anode material of SOFCs, which exhibits a high activity and durability for the electrochemical oxidation of CH_4 [26]. In this work, $La_{0.5}Ba_{0.5}Mn_{1-x}Co_xO_{3-\delta}$ (LBMCo) is studied as the cathode material of SOECs. The phase transition and the exsolution of Co during reduction are investigated. The effect of Co exsolution on the activity of the cathode for H_2O and CO_2 electrolysis is studied. The stability of the material is also examined.

2. Experimental

2.1. Preparation of materials

$La_{0.5}Ba_{0.5}MnO_{3-\delta}$ (LBM), $La_{0.5}Ba_{0.5}Mn_{0.9}Co_{0.1}O_{3-\delta}$ (LBM-1Co), $La_{0.5}Ba_{0.5}Mn_{0.8}Co_{0.2}O_{3-\delta}$ (LBM-2Co), $La_{0.5}Ba_{0.5}Mn_{0.7}Co_{0.3}O_{3-\delta}$ (LBM-3Co) and $La_{0.5}Ba_{0.5}Mn_{0.6}Co_{0.4}O_{3-\delta}$ (LBM-4Co) cathode powders were synthesized through the pechini method with $La(NO_3)_3\cdot 6H_2O$, $Ba(NO_3)_2$, $Mn(NO_3)_2$ and $Co(NO_3)_2\cdot 6H_2O$ as raw materials. Citric acid and ethylene glycol were used as complexation agents, and the detailed procedure was described in a previous work [26]. The powders were reduced in 5% H_2-95% Ar at various temperatures for characterization. $La_{0.4}Ce_{0.6}O_{2-\delta}$ (LDC) and $Ba_{0.5}Sr_{0.5}Co_{0.8}Fe_{0.2}O_{3-\delta}$ (BSCF) were used as cathode buffer layer and anode materials, respectively. The synthesis procedures can be find in previous publications [27-29].

2.2. Characterization

The X-ray diffraction (XRD) patterns of the cathode powders before and after reduction were recorded at room temperature with a D8 Focus diffractometer (Cu Kα radiation, Bruker) at a speed of 1.2° min^{-1}. The oxygen non-stoichiometries of the powders before reduction were measured with iodometry [30, 31]. The detailed procedure is described in the Supplementary Materials. The reduction processes of the powders were studied with thermogravimetric analysis (TGA) using a thermal analyzer (STA 449F3, Netzsch) in 5% H_2-95% Ar from 50 to 850 °C at a heating rate of 5 °C min^{-1}. The morphology of the powders was investigated with a scanning electron microscope (SEM, S-4800, Hitachi) and a transmission electron microscope (TEM, JEM-2100F, JEOL). CO_2 temperature programmed desorption (CO_2-TPD) curves of the cathode powders were measured to evaluate the adsorbing strength of the cathodes. The cathode powders of about 100 mg were reduced in H_2 at 850 °C for 2 h, and then cooled down to 50 °C in H_2. The powders were treated subsequently in CO_2 at 50 °C until the adsorption saturation was achieved. The samples were swept with Ar (50 ml min^{-1}) at 50 °C for 1 h, and then heated to 800 °C at a rate of 5 °C min^{-1}. The amount of CO_2 in Ar was detected with an online gas mass spectrometer (HPR20, Hiden).

2.3. Electrochemical tests

The oxygen surface exchange kinetics of the cathode materials was studied with the electrical conductivity relaxation (ECR) method. The powders were pressed into $30\times7.0\times2.0\ mm^3$ rectangular bars and sintered at 950 °C in air for 12 h subsequently. The electrical conductivity was measured with a four-probe direct current method. Fine Ag paste was added between the Ag leads and the porous bars to make a close contact. The samples were reduced in 5% H_2-95% Ar at 850 °C for 5 h before the test. Then the ECR process was investigated when the atmosphere was switched from 10% CO-90% CO_2 to 20% CO-80% CO_2 using an electrochemical workstation (VersaSTAT 3, Ametek).

The catalytic activities of the LBMCo materials were studied in electrolyte-supported symmetric cells and electrolysis cells. The $La_{0.8}Sr_{0.2}Ga_{0.8}Mg_{0.2}O_{3-\delta}$ (LSGM) electrolyte layer was fabricated by pressing the LSGM powder (Fuel cell materials) under 200 MPa and then sintered in air at 1450 °C for 20 h. The thickness of the LSGM layer was about 300 μm. The LBMCo, BSCF and LDC powders were mixed with V006 binder (Heraeus) to form slurries, respectively. For the LBMCo|LDC|LSGM|LDC|LBMCo symmetric cells, the LDC slurry was screenprinted on both sides of the electrolyte layer, followed by sintering at 1400 °C for 2 h. Then the LBMCo slurry was printed on the LDC layers, and the pellet was sintered in air at 950 °C for 4 h. The LBMCo|LDC|LSGM|BSCF electrolysis cells were fabricated through a similar process. The geometrical areas of the electrodes were 0.5 cm^2, and Ag paste was used as the current collector.

Before the electrochemical tests, the LBMCo electrodes were reduced at 850 °C in 5% H_2-95% Ar for 2 h. The electrochemical impedance spectra (EIS) of the symmetric cells were recorded from 1 MHz to 0.01 Hz with 10% H_2O-90% H_2 at both sides. For the H_2O and CO_2 electrolysis tests, the cathode gases were 10% H_2O-90% H_2 and 4% CO-96% CO_2, respectively, and air was used as the anode gas. The flow rates of the cathode and anode gases were all 100 ml min^{-1} (STP). *I-V* curves during the electrolysis processes were measured with the electrochemical workstation. The output gas was quantitatively analyzed with a gas chromatograph (Clarus 500, Perkin Elmer).

3. Results and discussion

3.1. Characterization

The $La_{0.5}Ba_{0.5}Mn_{1-x}Co_xO_{3-\delta}$ powders show a main cubic structure similar to $LaMnO_{3-\delta}$ phase (JCPDS51-1516) before reduction (Fig. 1a). A hexagonal phase corresponds to $BaMnO_{3-\delta}$ (JCPDS71-1521), which commonly exists in LBM synthesized in an oxidation atmosphere [32, 33], is observed when $x \leq 0.3$. A weak CoO_2 (JCPDS70-3469) peak is also detected in the samples containing Co. When x reaches 0.4, a hexagonal $BaCoO_{3-\delta}$ (JCPDS71-2453) phase is formed instead of $BaMnO_{3-\delta}$ and CoO_2. After LBM was reduced in 5% H_2-95% Ar at 850 °C for 5 h, the hexagonal phase is suppressed significantly (Fig. 1b), indicating the dissolution of $BaMnO_{3-\delta}$ in the main phase. Meanwhile, the main cubic phase turns to a tetragonal structure [26, 34], and weak MnO peaks (JCPDS75-0626) are also observed. With the doping of Co, the MnO phase disappears gradually, and the exsolution of metallic Co (JCPDS 89-4307) is detected. The Co peak becomes stronger with the increase of x from 0 to 0.3, indicating that more Co is exsolved. However, with further increase of Co content, LBM-4Co keeps the mixed cubic and $BaCoO_{3-\delta}$ phases after reduction, and metallic Co is not observed. The stability of the unreduced powders in CO_2 is also tested. After treated in pure CO_2 at 850 °C for 5 h, the powders keep the original structure when $x \leq 0.3$ (Fig. 1c). On the contrary, $BaCO_3$ is detected in LBM-4Co, indicating the poor chemical stability of the material. Therefore, LBM-4Co is not further studied in the following work.

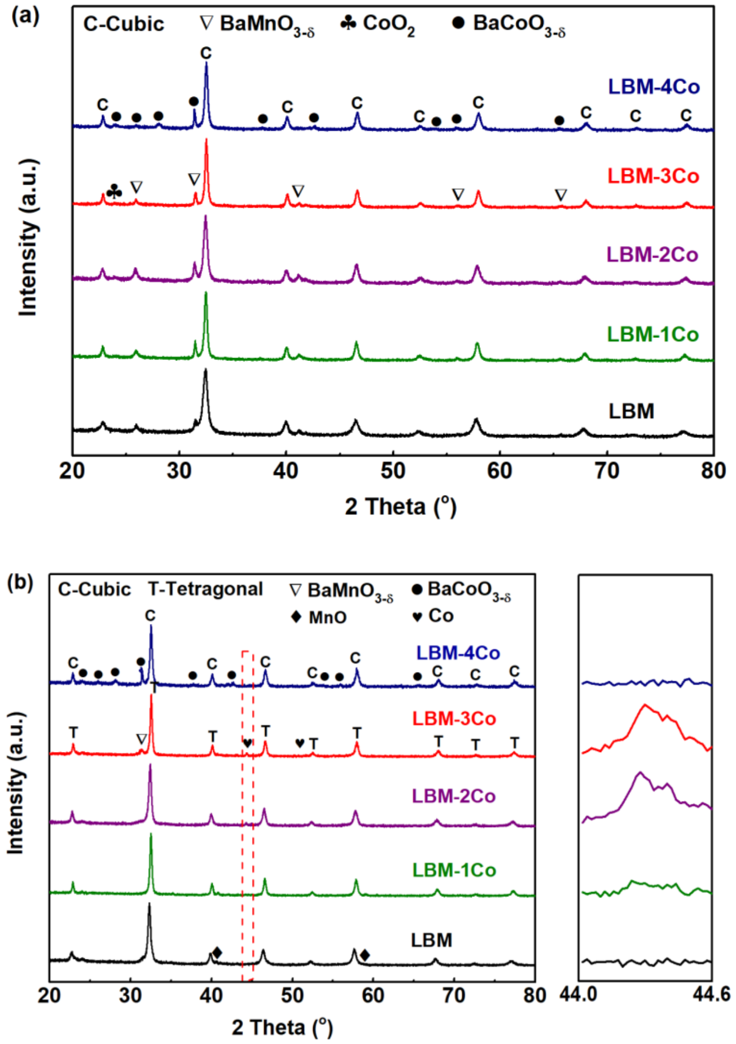

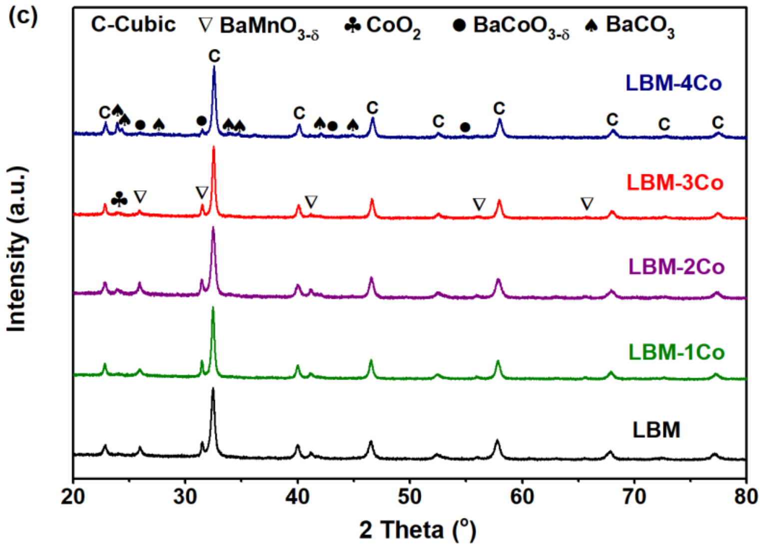

Fig. 1. XRD patterns of the cathode powders. (a) Before reduction; (b) After reduction in 5% H_2-95% Ar at 850 ºC for 5 h; (c) After treated in pure CO_2 at 850 ºC for 5 h (without pre-reduction).

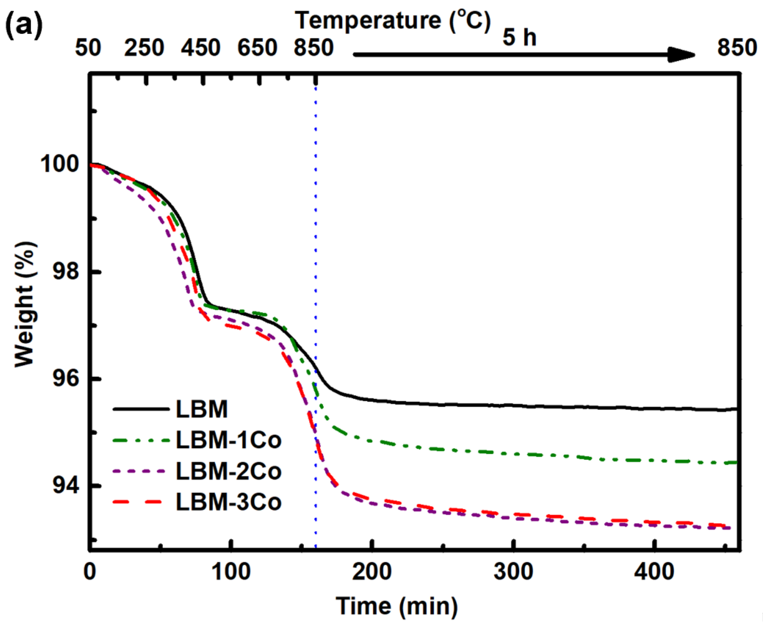

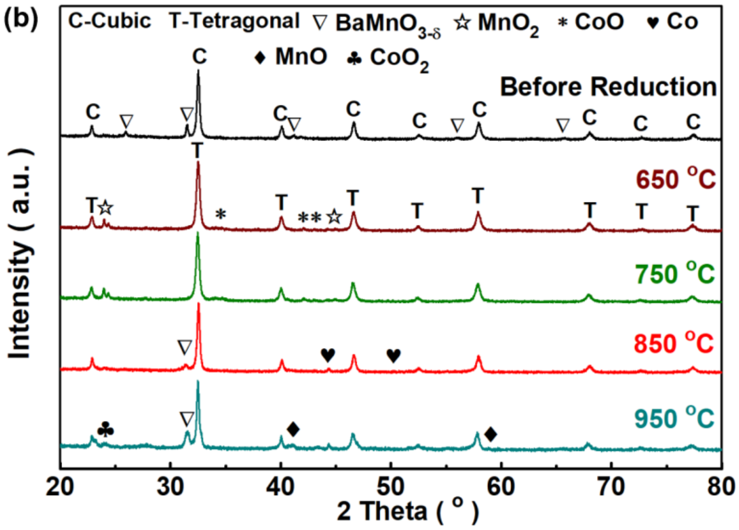

Fig. 2. (a) TGA results of the cathode powders in 5% H_2-95% Ar; (b) XRD patterns of LBM-3Co powder reduced in 5% H_2-95% Ar at various temperature for 5 h.

The concertation of oxygen vacancy (δ) in $La_{0.5}Ba_{0.5}Mn_{1-x}Co_xO_{3-\delta}$ powders in the oxidizing atmosphere is measured with iodometry. For LBM, LBM-1Co, LBM-2Co and LBM-3Co, the δ values are 0.01, 0.05, 0.10 and 0.11, respectively. The partial substitution of Mn by Co with a lower average valence brings more oxygen vacancies. The loss of lattice oxygen and the phase transition during reduction is studied with TGA in 5% H_2-95% Ar and in situ XRD (Fig. 2). Two major weight-loss steps are observed in the TGA curves. The weight losses of all the samples are similar in the first step from 200 to about 550 °C corresponding to the dissolution of $BaMnO_{3-\delta}$ and the transition of the main phase from the cubic to the tetragonal structure. MnO_2 (JCPDS12-0141) is also formed during that process. Meanwhile, the exsolution of CoO (JCPDS72-1474) is detected at 650 °C, which is further reduced to metallic Co in the second weight-loss step as the temperature goes up to 850 °C [35]. The loss of the weight during the second step generally increases with the increase of Co content, indicating the formation of more metallic Co. The exsolution of Co in the B-site promotes the dissolution of MnO_2.

Furthermore, the BaMnO$_{3-\delta}$ phase is re-formed with the loss of Co in the main phase, which is only observed in the samples with a high Co content (Fig. 1b). The XRD peaks of BaMnO$_{3-\delta}$ and Co become stronger when the reducing temperature is further raised to 950 °C. In the meantime, other phases such as CoO$_2$ and MnO are observed, implying the gradual decomposition of the main phase.

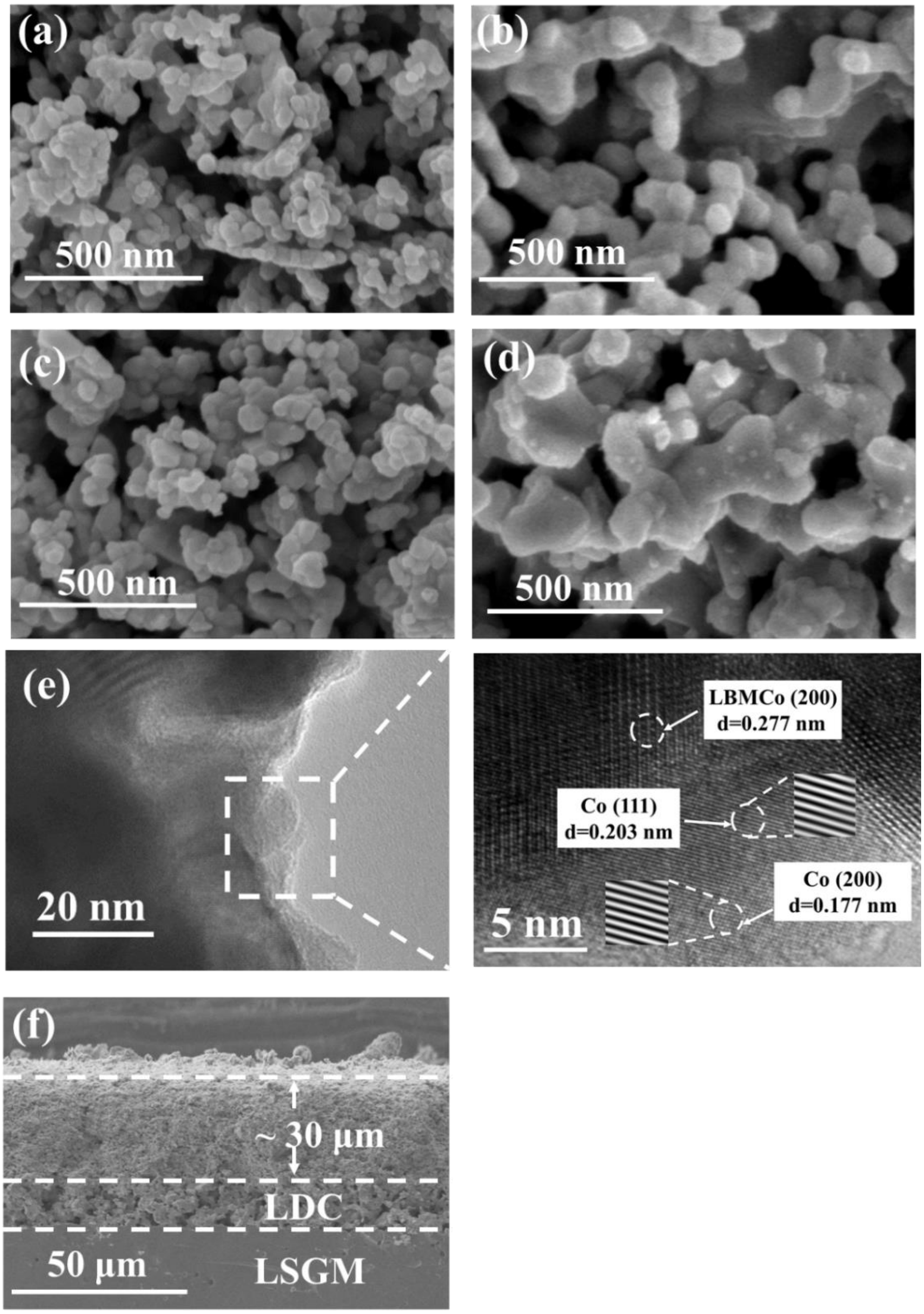

Fig. 3. SEM images of (a) unreduced LBM powder, (b) reduced LBM powder, (c) unreduced LBM-3Co powder, (d) reduced LBM-3Co powder; (e) TEM image of reduced LBM-3Co powder (left) and its magnified image (right); (f) cross-sectional SEM image of a electrolysis cell at the cathode side.

The LBM anode powder is composed of particles with an average diameter of about 50 nm in the oxidizing atmosphere (Fig. 3a), and a moderate aggregation is observed after reduction (Fig. 3b). The LBM-3Co powder (Fig. 3c) shows a similar morphology to LBM before reduction, while numerous 10 nm-diameter particles are exsolved after the treatment in 5% H_2-95% Ar at 850 ºC for 5 h (Fig. 3d). The high-resolution TEM image of the reduced LBM-3Co powder is shown in Fig. 3e. (2 0 0) planes of LBMCo with a lattice space of 0.277 nm are found in the main phase, and the interplanar spacings of 0.177 and 0.203 nm in the nanoparticle are corresponding to the (2 0 0) and (1 1 1) planes in Co, respectively, consistent with the XRD result that Co is exsolved from LBM-3Co after reduction. The thicknesses of the anode layer and the LDC interlayer in a single cell are about 30 and 10 μm, respectively (Fig. 3f). The porous interlayer adheres to the porous anode layer and the dense LSGM electrolyte tightly. The CO_2-TPD results of the cathode powders are shown in Fig. 4. The peaks between 250-270 ºC are from CO_2 physically adsorbed on the samples, and those above 600 ºC are chemically adsorbed CO_2. With the doping of Co in the cathode, the CO_2 desorption temperature increases, suggesting the increase of CO_2 adsorbing strength.

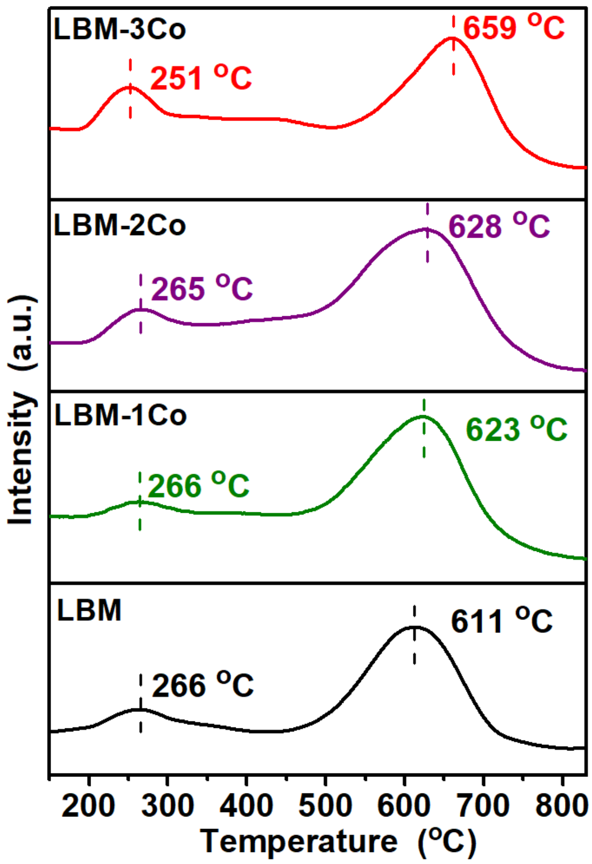

Fig. 4. CO_2-TPD curves of the cathode powders.

3.2. Electrochemical performance

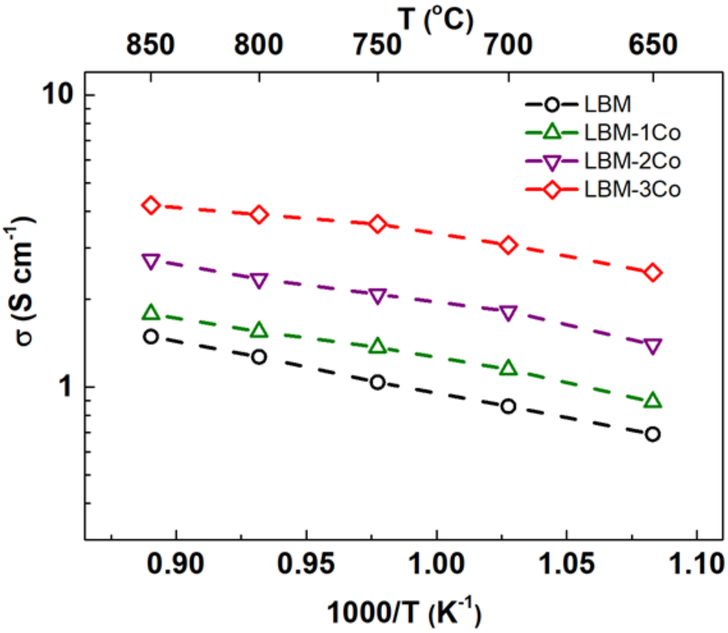

Fig. 5. Electrical conductivities of the cathode materials sintered at 950 °C measured in 10% CO-90% CO_2 mixture.

The electrical conductivities of the LBMCo bars in 10% CO-90% CO_2 mixture is shown in Fig. 5. The relative densities of the samples sintered at 950 °C in air are about 60% measured by Archimedes method, and the reducing process further increases the porosities of the samples. The conductivity increases with the rise of temperature and the increase of Co in the sample. The electrical conductivities of LBM, LBM-1Co, LBM-2Co and LBM 3Co porous bars are about 1.5, 1.8, 2.7 and 4.2 S cm^{-1} at 850 °C, respectively. The conductivity drops when the atmosphere is changed to 20% CO-80% CO_2, indicating a p-type conducting behavior. The normalized conductivity curves measured when the atmosphere is changed from 20% CO-80% CO_2 to 10% CO-90% CO_2 is shown in Fig. 6a. The re-equilibrium time of the LBM sample is about 1800 s at 700 °C, which is reduced to about 400 s at 850 °C. The ECR process generally becomes quicker with more Co in the sample, and it takes about 250 s for both LBM-2Co and LBM-3Co at 850 °C. The ECR behavior is determined by the oxygen transport processes, *i.e.* the surface reaction and the bulk diffusion [36]. In this work, the bulk diffusion length in the samples with a porosity higher than 40% should be very short, and the ECR process is mainly influenced by the surface exchange coefficient (k), as described in Equation 1 [37, 38].

$$\frac{\sigma(t)-\sigma(0)}{\sigma(\infty)-\sigma(0)} = 1 - \exp\left(-\frac{kt}{\alpha}\right) \qquad (1)$$

Where t is the time of relaxation, $\sigma(0)$ and $\sigma(\infty)$ are the initial and final conductivities of the sample, and α represents the diffusion length. Unlike the measurements with dense samples, it is difficult to determine α and k of the porous bars in this work directly. However, the values of k/α at various temperatures are obtained based on the ECR results, and the activation energy (Ea) of the surface reaction is calculated subsequently. As shown in Fig. 6b, with the increase of Co content, *E*a decreases gradually from 1.08 eV (LBM) to 0.79 eV (LBM-3Co). The exsolved Co nanoparticles can increase the adsorbing strength of CO_2 (Fig. 4) and facilitate the surface exchange of oxygen, resulting in a lower *E*a.

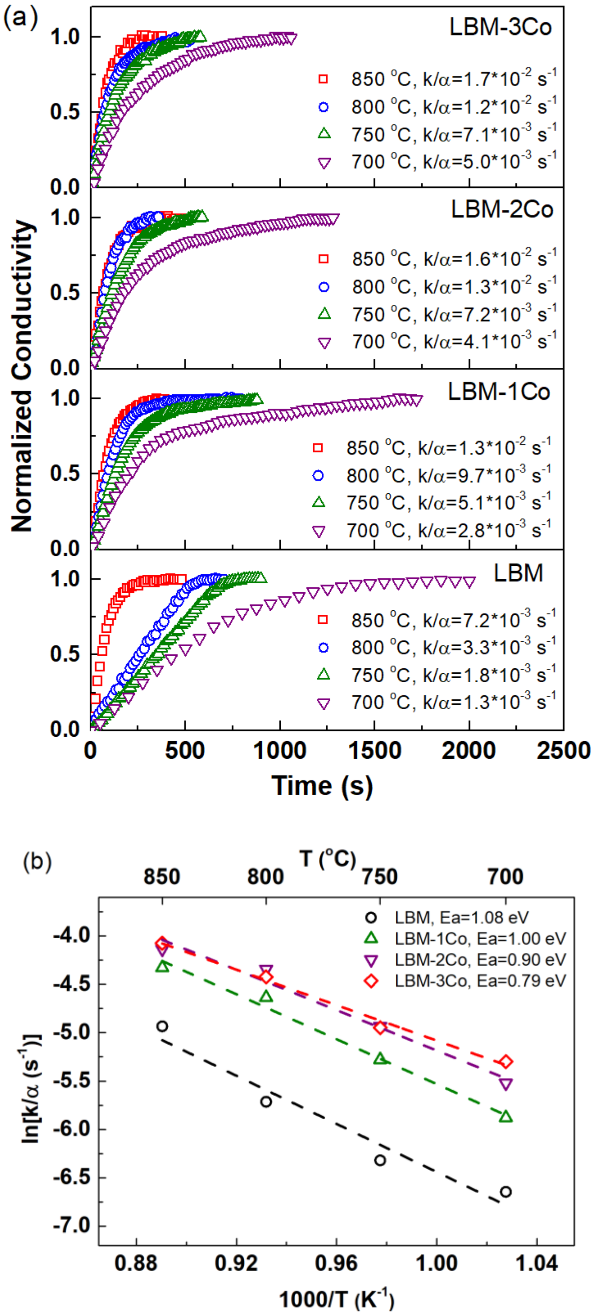

Fig. 6. (a) Electrical conductivity relaxation results and (b) *k*/*α* values of the porous bars at various temperatures.

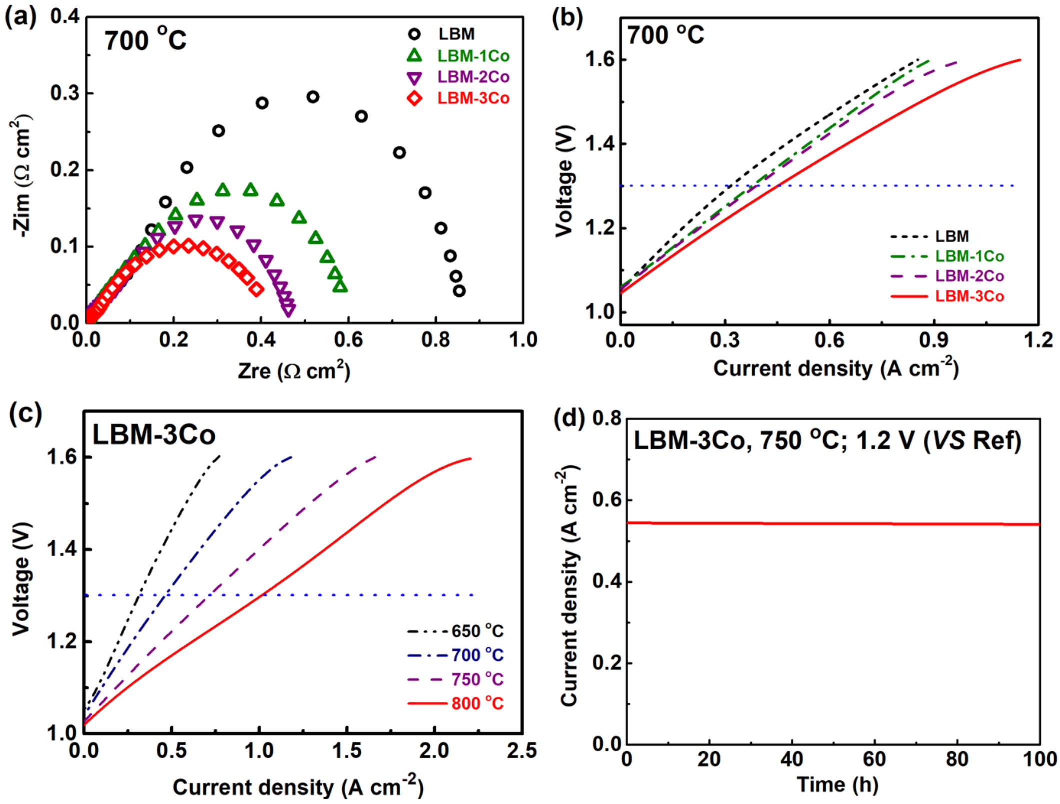

Fig. 7. (a) EIS curves of the symmetric cells with 90% H_2-10% H_2O at both sides at 700 °C; (b) H_2O electrolysis curves of the cells with different cathodes at 700 °C; (c) H_2O electrolysis curves of the cell with LBM-3Co cathode at various temperatures; (d) stability of the H_2O electrolysis cell with LBM-3Co cathode under an operating voltage of 1.2 V at 750 °C.

The EIS curves of the symmetric cells at 700 °C with 10% H_2O-90% H_2 at both sides are presented in Fig. 7a. The arcs correspond to the electrode polarization resistances (R_p), while the ohmic resistances of the cells are deducted for comparison. R_p decreases with the increase of Co in the electrode, and LBM-3Co shows the lowest R_p of about 0.4 Ω cm^2 due to the fast surface exchange of oxygen. Fig. 7b shows the electrolysis curves of the cells with different cathodes. The open circuit voltages

(OCVs) of the cells are around 1.03-1.05 V, close to the theoretical potential. The electrolysis performance is improved when Co is added in the cathode. With an applied voltage of 1.3 V, the electrolysis current density of the cell with LBM cathode is 0.32 A cm^{-2}, and that with LBM-3Co cathode reaches 0.46 A cm^{-2}, which is attributed to the high electrical conductivity and the high catalytic activity of LBM-3Co. The electrolysis current increases with the rise of temperature. The current densities of the LBM-3Co cell at 1.3 V are 0.31, 0.46, 0.71 and 1.01 A cm^{-2} at 650, 700, 750 and 800 ºC, respectively (Fig. 7c). The stability of the electrolysis cell is tested at 750 ºC with an operating voltage of 1.2 V. The electrolysis current keeps constant for 100 h (Fig. 7d), demonstrating a high durability of the cathode material and the cell.

Table 1. Current densities of the CO_2 electrolysis cells with high-performance cathodes.

Cathode	Fuel composition	OCV (V)	Current density (A cm^{-2})		Ref.
			0.3 V (vs. OCV)	1.2 V (operating potential)	
Ni-11% MnO_x	2% CO-80% CO_2-18% Ar	0.5	0.3	1.1	[15]
Ni-YSZ-3% MnO_x	2% CO-80% CO_2-18% Ar	0.4	0.2	1.0	[15]
Ni-Cr_2O_3		0.4	0.3	0.8	[5]
NiFe-$La_{0.6}Sr_{0.4}Fe_{0.8}Mn_{0.2}O_3$	1% CO-50% CO_2-49% Ar	0.8	0.1	0.3	[7]
NiCu-$La_{0.75}Sr_{0.25}Cr_{0.5}Mn_{0.5}O_3$-$Ce_{0.8}Sm_{0.2}O_{1.9}$	Pure CO_2	0.8	0.2	0.3	[6]
$La_{0.8}Sr_{0.2}FeO_{3-\delta}$-$Ce_{0.8}Sm_{0.2}O_{1.9}$	Pure CO_2	0.1	0.3	0.6	[8]
$Sr_2Fe_{1.5}Mo_{0.5}O_{6-\delta}$-$Ce_{0.8}Sm_{0.2}O_{1.9}$	Pure CO_2	0.1	0.2	0.6	[10]
$Sr_2Fe_{1.5}Mo_{0.5}O_{6-\delta}F_{0.1}$	Pure CO_2	0.1	0.2	0.8	[12]
$La_{0.6}Sr_{0.4}Mn_{0.3}Co_{0.7}O_{3-\delta}$	30% CO-70% CO_2	0.9	0.3	0.3	[21]
$La_{0.5}Ba_{0.5}Mn_{0.7}Co_{0.3}O_{3-\delta}$	4% CO-96% CO_2	0.83	0.45	0.6	This work

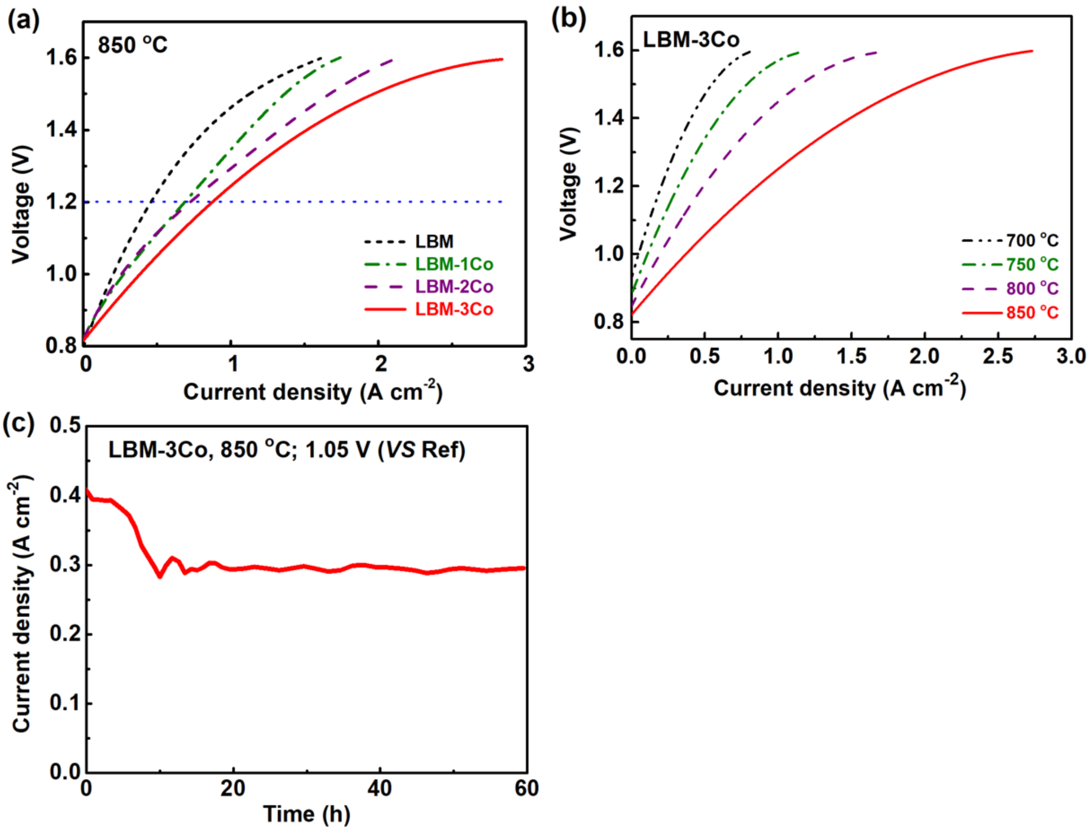

Fig. 8. (a) CO_2 electrolysis curves of the cells with different cathodes at 850 °C; (b) CO_2 electrolysis curves of the cell with LBM-3Co cathode at various temperatures; (c) Durability of the CO_2 electrolysis cell with LBM-3Co cathode under an operating voltage of 1.05 V at 850 °C.

The CO_2 electrolysis results of the cells at 850 °C are shown in Fig. 8a. The OCV of the cells are around 0.80-0.82 V. Similar to the H_2O electrolysis, the CO_2 electrolysis activity of the cathode is also improved with the addition of Co. The current density of the LBM cell is 0.46 A cm^{-2} at 1.2 V, and increases to 0.88 A cm^{-2} when the cathode is replaced by LBM-3Co. The CO_2 electrolysis performance of the single cells supported by 250-300 μm-thick LSGM electrolyte layers at 800 °C reported recently are listed in Table 1. With various atmospheres at the fuel side, the OCV of the electrolysis cells ranges from 0.1 to 0.9 V, and it is more appropriate to evaluate the cathode activity by comparing the electrolysis currents under the same applied voltage (the potential *vs.* OCV) instead of the same operating potential. The OCV of the cell with LBM-3Co cathode is about 0.83 V at 800 ºC (Fig. 8b). With an applied voltage of 0.3 V, the CO_2 electrolysis current density reaches 0.45 A cm^{-2}, much higher than the cells with other excellent cathode materials, demonstrating a high activity of the LBM-3Co cathode. The CO_2 electrolysis stability at 850 ºC with an operating voltage of 1.05 V is shown in Fig. 8c. The electrolysis current decreases from 0.4 A cm^{-2} to 0.3 A cm^{-2} during the first 10 h. The switch of the cathode gas from 5% H_2-95% Ar to 4% CO-96% CO_2 at 850 ºC results in the increase of the oxygen partial pressure from about 10^{-25} to 10^{-15} atm, which leads to the partly re-oxidation of the exsolved Co and the decrease of the cathode activity. The current density is almost stable in the next 50 h, and the quantitative analysis of CO in the outlet gas demonstrates a coulombic efficiency over 90%.

Finally, the co-electrolysis of H_2O and CO_2 using the Co-exsolved cathode is briefly studied. The OCVs of the single cells with 4% CO-86% CO_2-10% H_2O as the cathode gas are about 0.80-0.83 V at 800 ºC (Fig. 9a). The co-electrolysis current is slightly higher than the CO_2-electrolysis current. The production of H_2 and CO and co-electrolysis current rise with the increase of the operating voltage (Fig. 9b), and the Faradaic efficiencies at various voltages are about 95%. The ratio between CO and H_2 in the product is around 2.3-2.6. The high partial pressure of CO_2 in the cathode gas facilitates its adsorption and surface reaction, resulting in more CO. The endothermic reversed water-gas shift reaction promoted by the high operating temperature and the high content of CO_2 is another probable source of CO. The CO/H_2 ratio can be further controlled by adjusting the amounts of CO_2 and H_2O in the reactant gas and the operating temperature.

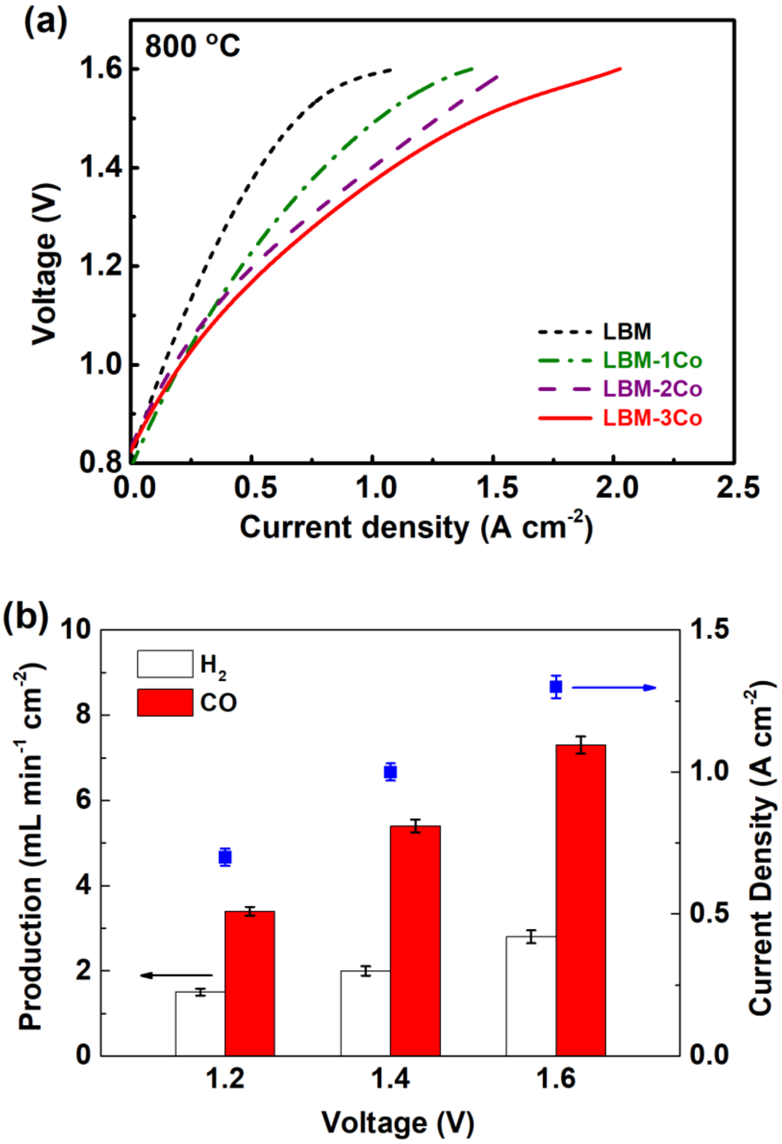

Fig. 9. (a) H_2O-CO_2 co-electrolysis curves of the cells with various cathodes at 800 °C; (b) Productions of H_2 and CO and the current densities of the cell with LBM-3Co cathode under different operating voltages.

4. Conclusions

In this work, $La_{0.5}Ba_{0.5}Mn_{1-x}Co_xO_{3-\delta}$ is synthesized through the pechini method and studied as the cathode material for H_2O and CO_2 SOECs. The cathode exhibits a main cubic structure in an oxidizing atmosphere, and changes to a tetragonal structure with in situ exsolved Co nanoparticles after reduction at 850 °C when x is not higher than 0.3. The doping of Co increases the electrical conductivity of LBM in a reducing atmosphere. The metallic Co nanoparticles also facilitate the surface oxygen exchange reaction, resulting in a high catalytic activity. With LBM-3Co cathode and a 300 μm-thick LSGM electrolyte layer, the single cell electrolyzing H_2O exhibits 0.46 and 1.01 A cm^{-2} at 700 and 800 °C, respectively, with an operating voltage of 1.3 V. With the same cathode, A CO_2 electrolysis current density of 0.88 A cm^{-2} and a Faradaic efficiency over 90% are achieved at 1.2 V and 850 °C. The cell shows a good durability during the electrolysis of both H_2O and CO_2. The co-electrolysis of H_2O and CO_2 is also realized with the cathode, and a high CO_2 content in the reactant gas leads to a high CO/H_2 ratio in the product.

Acknowledgements

The financial support of Tianjin Municipal Science and Technology Commission under contract number 19JCYBJC21700 and the support of NSF of China under contract number 51402210 are gratefully acknowledged. The work has been also supported by the Program of Introducing Talents to the University Disciplines under file number B06006, and the Program for Changjiang Scholars and Innovative Research Teams in Universities under file number IRT 0641.

References

[1] S.D. Ebbesen, S.H. Jensen, A. Hauch, M.B. Mogensen, Chem. Rev. 114 (2014) 10697-10734.

[2] L. Bi, S. Boulfrad, E. Traversa, Chem. Soc. Rev. 43 (2014) 8255-8270.

[3] Y. Zheng, J.C. Wang, B. Yu, W.Q. Zhang, J. Chen, J.L. Qiao, J.J. Zhang, Chem. Soc. Rev. 46 (2017) 1427-1463.

[4] V. Kyriakou, D. Neagu, E.I. Papaioannou, I.S. Metcalfe, M.C.M. van de Sanden, M.N. Tsampas, Appl. Catal., B 258 (2019) 117950.

[5] X.L. Hu, K. Xie, J. Power Sources 430 (2019) 20-24.

[6] C.L. Zhu, L.X. Hou, S.S. Li, L.Z. Gan, K. Xie, J. Power Sources 363 (2017) 177-184.

[7] S.J. Wang, H. Tsuruta, M. Asanuma, T. Ishihara, Adv. Energy Mater. 5 (2015) 1401003.

[8] Y. Yang, Y.H. Li, Y.N. Jiang, M.H. Zheng, T. Hong, X.J. Wu, C.R. Xia, Electrochim. Acta 284 (2018) 159-167.

[9] L.Z. Bian, C.C. Duan, L.J. Wang, Y.T. Hou, L.Z. Zhu, R. O'Hayre, K.C. Chou, J. Electrochem. Soc. 165 (2018) F981-F985.

[10] Y.H. Li, X.R. Chen, Y. Yang, Y.N. Jiang, C.R. Xia, ACS Sustainable Chem. Eng. 5 (2017) 11403-11412.

[11] S. S. Hou, K. Xie, Electrochim. Acta 301 (2019) 63-68.

[12] Y.H. Li, Y. Li, Y.H. Wan, Y. Xie, J.F. Zhu, H.B. Pan, X.S. Zheng, C.R. Xia, Adv. Energy Mater. 9 (2019) 1803156.

[13] J.H. Myung, D. Neagu, D.N. Miller, J.T.S. Irvine, Nature 537 (2016) 528-531.

[14] J.T.S. Irvine, D. Neagu, M.C. Verbraeken, C. Chatzichristodoulou, C. Graves, M.B. Mogensen, Nat. Energy 1 (2016) 15014.

[15] W.Y. Wang, L.Z. Gan, J.P. Lemmon, F.L. Chen, J.T.S. Irvine, K. Xie, Nat. Commun. 10 (2019) 1550.

[16] G. Tsekouras, D. Neagu, J.T.S. Irvine, Energy Environ. Sci. 6 (2013) 256-266.

[17] L.T. Ye, M.Y. Zhang, P. Huang, G.C. Guo, M.C. Hong, C.S. Li, J.T.S. Irvine, K. Xie, Nat. Commun. 8 (2017) 14785.

[18] J.H. Lu, C.L. Zhu, C.C. Pan, W.L. Lin, J.P. Lemmon, F.L. Chen, C.S. Li, K. Xie, Sci. Adv. 4 (2018) eaar5100.

[19] M. Chanthanumataporn, J.N. Hui, X.L.Yue, K. Kakinuma, J.T.S. Irvine, K. Hanamura, Electrochim. Acta 306 (2019) 159-166.

[20] D.J. Deka, S. Gunduz, T. Fitzgerald, J.T. Miller, A.C. Co, U.S. Ozkan, Appl. Catal., B 248 (2019) 487-503.

[21] S. Park, Y. Kim, H. Han, Y.S. Chung, W. Yoon, J. Choi, W.B. Kim, Appl. Catal., B 248 (2019) 147-156.

[22] S.B. Liu, Q.X. Liu, J.L. Luo, J. Mater. Chem. A 4 (2016) 17521-17528.

[23] S. Sengodan, S. Choi, A. Jun, T.H. Shin, Y.W. Ju, H.Y. Jeong, J. Shin, J.T.S. Irvine, G. Kim, Nat. Mater. 14 (2015) 205-209.

[24] A. Jun, J. Kim, J. Shin, G. Kim, Angew. Chem. Int. Ed. Engl. 55 (2016) 12512-12515.

[25] T.H. Shin, J.H. Myung, M. Verbraeken, G. Kim, J.T.S. Irvine, Faraday Discuss. 182 (2015) 227-239.

[26] N.J. Hou, T.T. Yao, P. Li, X.L. Yao, T. Gan, L.J. Fan, J. Wang, X.J. Zhi, Y.C. Zhao, Y.D. Li, ACS Appl. Mater. Interfaces 11 (2019) 6995-7005.

[27] Z.P. Shao, S.M. Haile, Nature 431 (2004) 170-173.

[28] Z.P. Shao, W.S. Yang, Y. Cong, H. Dong, J.H. Tong, G.X. Xiong, J. Membrane Sci. 172 (2000) 177-188.

[29] H. Sato, S. Hashimoto, T. Nakamura, K. Yashiro, K. Amezawa, T. Kawada, ECS Trans. 57 (2013) 1125-1133.

[30] Y. Song, Q. Zhong, W.Y. Tan, C. Pan, Electrochim. Acta 139 (2014) 13-20.

[31] T.T. Yao, N.J. Hou, J.J. Gan, J. Wang, X.J. Zhi, L.J. Fan, T. Gan, Y.C. Zhao, Y.D. Li, J. Power Sources 425 (2019) 103-109.

[32] J. Spooren, R.I. Walton, F. Millange, J. Mater. Chem. 15 (2005) 1542-1551.

[33] T. Nakajima, H. Kageyama, H. Yoshizawa, K. Ohoyama, Y. Ueda, J. Phys. Soc. Jpn. 72 (2003) 3237-3242.

[34] F. Millange, V. Caignaert, B. Domenges, B. Raveau, E. Suard, Chem. Mater. 10 (1998) 1974-1983.

[35] K.Y. Lai, A. Manthiram, Chem. Mater. 30 (2018) 2838-2847.

[36] I. Yasuda, T. Hikita, J. Electrochem. Soc. 141 (1994) 1268-1273.

[37] M.H. Zheng, S. Wang, M. Li, C.R. Xia, J. Power Sources 345 (2017) 165-175.

[38] T. Ishihara, J.A. Kilner, M. Honda, N. Sakai, H. Yokokawa, Y. Takita, Solid State Ionics 113 (1998) 593-600.